Developing an AFM-Based SECM System; Instrumental Setup, SECM Simulation, Characterization, and Calibration

A. Davoodi,[a,c,*,z] A. Farzadi,[b] J. Pan,[a,**] C. Leygraf,[a,**] and Y. Zhu[d]

[a]Division of Corrosion Science, Department of Chemistry, and [b]Department of Mechanics, School of Engineering Sciences, Royal Institute of Technology, SE-100 44 Stockholm, Sweden
[c]Department of Materials Engineering, Tarbiat Moallem University of Sabzevar, 397, Sabzevar, Khorasan, Iran
[d]Windsor Scientific Limited, Slough, SL1 4HE, United Kingdom

An integrated atomic force microscopy/scanning electrochemical microscopy (AFM/SECM) system was developed as an in situ local electrochemical probing technique. It consists of a dual-mode probe acting as an AFM cantilever and SECM microelectrode to simultaneously obtain the topography and electrochemical current map of the same area. Two types of probes with different geometries were used. The scan velocity and concentration profile of the redox mediator during the scan were simulated, using the equations of convection–diffusion mass transport coupled with continuity and momentum in three dimensions under steady-state and transient conditions. The temporal and spatial resolutions of the probes were investigated. It was found that, during a normal scan rate (around 1 Hz), the effect of convective transport is negligible and the SECM lateral resolution depends on the geometrical parameters. With favorable geometry, a probe with a Pt microelectrode of 1 μm diameter can distinguish two active sites with a distance of at least 3–4 μm. The paper also reports experiments for characterization and calibration of the AFM/SECM system. Concurrent AFM and SECM images obtained on a gold band calibration sample verify the high-resolution capability of the SECM of one or a few micrometers with optimized conditions.
© 2008 The Electrochemical Society. [DOI: 10.1149/1.2943324] All rights reserved.

In recent years, both atomic force microscopy (AFM) and scanning electrochemical microscopy (SECM) have been applied to investigate localized electrochemical events such as biosensor, catalytic activity, localized corrosion, etc.[1-23] AFM gives high-resolution topographic information, and is able to precisely control the distance between the sample and the probe, whereas SECM can provide detailed information of local electrochemical activities due to anodic and cathodic processes. SECM results can give valuable information on chemical and electrochemical changes above and around local active sites which can indirectly be an indication of local activity variation related to local surface activities due to its heterogeneous microstructure. Despite many successful applications, the spatial resolution of SECM is lower than that of scanning probe microscopy-based techniques such as AFM.[13] Therefore, a low lateral resolution of SECM current imaging was a crucial issue. However, usually AFM lacks chemical specificity. Attempts were made to solve the problem in different ways. Great efforts were made to improve the spatial resolution of SECM by using AFM distance control capability, which permits high-resolution data acquisition.

Different approaches have been reported for producing a bifunctional probe acting simultaneously as an AFM tip and SECM microelectrode. Macpherson et al. reported the integration of an SECM/AFM probe achieved by using a photolithography method.[13,14] In this case, an oxide sharpened silicon nitride (Si_3N_4) AFM tip was used and the gold-coated AFM cantilever was insulated with photoresist coating. Illuminating with an optical micropattern generator opened the end point of the AFM tip for the SECM signal. This type of probe was also used in dynamic force microscopy with magnetic field excitation to recognize the enzymatic activities of a glucose biosensor.[24] Moreover, the SECM/AFM Si_3N_4 cantilever was combined with integrated pyramidal tips.[18,19] The underside of the probe was sputter coated with Cr and Pt to provide conducting AFM tips capable of functioning as electrodes, as well as force sensors. The electrochemical and electrical properties of dimensionally stable $Ti/TiO_2/Pt$ electrodes have been investigated using this type of probe.[18,19]

In another approach, a combined SECM/AFM probe was fabricated by a coating flattened and etched Pt microwire with electrophoretically deposited paint for insulation.[14-16] The steps involved in the fabrication of SECM-AFM tips were (*i*) constructing a Pt microwire electrode, (*ii*) etching the Pt to a small point, (*iii*) fabricating the cantilever component of the SECM-AFM tip by compression, (*iv*) insulating the electrode and cantilever by electrodeposition of a paint, which retracts from the tip end during heat curing to expose a small Pt electrode, and (*v*) fixating the probe to the AFM holder using epoxy resin.[16-19] Meanwhile, Kranz et al. presented an approach to fabricate a microelectrode integrated in a standard AFM tip.[20-22] The sequences of fabrication were (*i*) metal (Cr and Au) coating of the Si_3N_4 cantilever by sputtering, (*ii*) insulating (with a silicon nitride layer) of the metal-coated AFM cantilever by plasma-enhanced chemical vapor deposition, and (*iii*) focused ion beam (FIB) cutting of the modified AFM cantilever. Simultaneous contact mode imaging of a micropatterned sample with immobilized enzyme spots and imaging of enzyme activity was obtained using this type of probe.[22] More recently, by using nanofabrication facilities including several ionic and chemical etching steps of Si wafer and following low-pressure chemical vapor deposition of silicon nitride (Si_3N_4) and Pt, a platinum silicide (Pt_xSi_x) tip was produced for a bifunctional AFM/SECM probe.[23] Moreover, taking advantage of metal masking technology and FIB, a precise exposure of Pt-coated silicon nitride AFM tip could be achieved to fabricate an array of SECM/AFM probes.[25]

To determine the benefits of integrated SECM/AFM measurements, various numerical simulation methods have been employed for the SECM part.[26-33] The simulation of SECM could assist in the analysis of the influence of different electrochemical and geometrical parameters on the experimental performance, such as the resolution. For instance, to estimate and improve the resolution of SECM, one can use simulations to study the influence of geometrical parameters. Because the fabrication of bifunctional AFM/SECM probes still is a challenging and expensive process, simulation could also help to evaluate the performance and improve the probe design.

An adaptive finite element algorithm was used for simulation of arbitrarily shaped SECM tips in two dimensions.[26,27] Steady-state and transient amperometric SECM responses were simulated in three dimensions with the boundary element method (BEM).[28,30-33] The SECM amperometric experiments with a heptode microelectrode (a Pt core microelectrode surrounded by quartz glass and six microelectrodes at premier) as a local probe were quantitatively analyzed by means of three-dimensional (3D) numerical simulations

with the BEM. The numerical simulation was used for analysis of SECM linescan experiments to determine the spatial resolution.[30] Lateral resolution of SECM imaging with a 25 μm-sized Pt electrode on two enzyme beads with 236 μm distance was simulated by BEM. The results showed that, if the enzyme loading differs by more than a factor of 2, a large spacing is required to allow the identification of two spots.[33] Furthermore, a frame-shaped integrated AFM/SECM probe fabrication was combined with 3D BEM simulation to facilitate the SECM imaging of nanodomains in, e.g., biological systems.[32] Moreover, the finite element method (FEM) has been employed for characterization of a microfabricated SECM/AFM probe.[16] Simulations and experiments were performed for flux generation at an uninsulated metal-coated AFM/SECM probe.[29] It was shown through simulation that a high spatial resolution could be achieved by employing short generation times. The accuracy of the simulations was confirmed by generation–collection measurements.[29] Advective and transient effects of combined AFM/SECM operations were investigated by the finite volume method. The results showed that purely diffusional steady-state equations can be used for the particular AFM/SECM frame electrode geometry with a scan rate of 1–10 μm s^{-1}.[34] However, the velocity used was quite slow, and to our knowledge there is no report in the literature concerning application of FEM on the SECM resolution issue, specifically the effect of convection for a very fast scan rate (up to ca. 700 μm s^{-1}).

Recently, we have applied an integrated SECM/AFM system for in situ investigation of localized corrosion of Al alloys.[2,35-38] In this work, to combine the benefits of the two techniques, an integrated AFM/SECM system has been developed as an in situ local electrochemical technique. To aid in the interpretation of the results, numerical simulation of the SECM current mapping was performed to analyze the spatial resolution and the influencing parameters. This paper describes the instrumental setup and reports the FEM simulation of the SECM operation using two different probe configurations. The temporal and spatial resolutions are discussed, focusing on the influence of the sample–tip distance, tip diameter, size of active sites on the sample surface, and the distance between them. Meanwhile, to evaluate the influence of the probe scan rate, convection–diffusion mass transport equations coupled with continuity and momentum equations have been solved numerically and the contribution of convective transport on probe performance was analyzed.

The present paper also reports the experimental studies for characterization and calibration of the AFM and SECM system, and verification of the resolution through probing a gold band calibration sample using two types of probes with different geometrical configurations. Because the calibration sample used did not give the highest possible resolution distinction (the reason was that each gold band had a minimum 10 μm width), the simulation tool has been mostly employed for probe geometry design optimization.

Simulation and Experimental Setup, Sample, and Solution

AFM/SECM measurement setup and principle.— Figure 1a shows the schematics of an AFM-based SECM instrument. By using a three-electrode electrochemical cell and a bipotentiostat, the potential of the sample and of the microelectrode (an embedded Pt wire) in the dual-mode probe was controlled separately with respect to a reference electrode, and a Pt sheet surrounding the sample acted as the counter electrode. A laser feedback outside of the solution as a deflection control was operating for normal AFM topography data acquisition. During the SECM operation, the distance was kept constant at the micrometer and submicrometer level between the sample surface and the probe (Pt microelectrode). This gives a great advantage over normal SECM instruments where the distance control is difficult to achieve and scratching the surface frequently occurs. By using this configuration concurrent topography and electrochemical activity could be monitored.

Figure 1b illustrates the principle of the dual-mode AFM/SECM measurements in this study. In the integrated AFM/SECM measure-
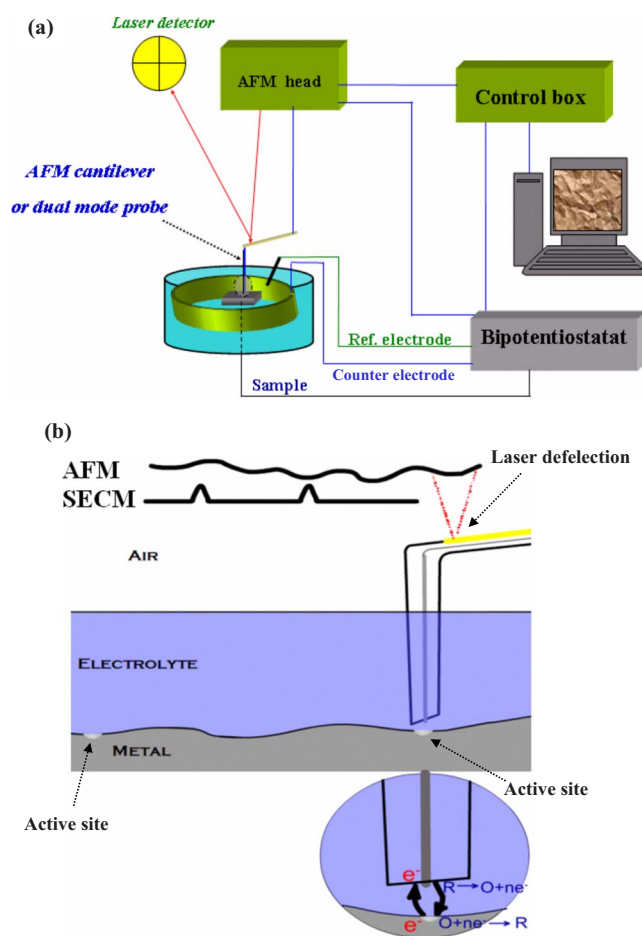

Figure 1. (Color online) (a) Schematic of electrochemical AFM/SECM experiment setup and (b) principle of dual-mode AFM/SECM measurement.

ments, after a normal AFM linescan to obtain a surface profile in the first pass, the feedback was stopped and the tip withdrawn to a desired distance (a few nm to a few micrometers) from the surface as shown in Fig. 1b. In the second pass, the probe followed the surface profile in the second linescan with a constant lift-up distance, and collected the local current. This means that the integrated AFM/SECM mapping takes approximately twice the time compared to normal AFM imaging. Clearly, the lift-up distance should be optimized. It should not be too far from the surface to lose the resolution, whereas it should not be too close to the surface so that no direct electrical contact between the Pt microelectrode and the metallic sample surface is avoided. This distance also prevents damage of the whole probe, particularly the Pt microelectrode during scanning. By using the integrated AFM/SECM system, concurrent AFM topography and SECM current maps were obtained on exactly the same area with a high lateral resolution.

In general, using the redox couple as a mediator, the SECM measurement can be performed either in feedback mode (described later) or in generation–collection mode as follows[39,40]

$$O + ne^- \rightarrow R \quad (\text{Pt microelectrode}) \quad [1]$$

$$R \rightarrow O \rightarrow ne^- \quad (\text{substrate}) \quad [2]$$

O and R represent the oxidized and reduced species, respectively. More details on SECM principle can also be seen in Ref. 39 and 40.

Probe geometry and simulation domain.— Two types of dual-mode AFM/SECM probes, supplied by Windsor Scientific Ltd, U.K., were used in this study.[2,35-38] Figures 2a and b show a scanning electron microscopy (SEM) micrograph of probe A and a con-
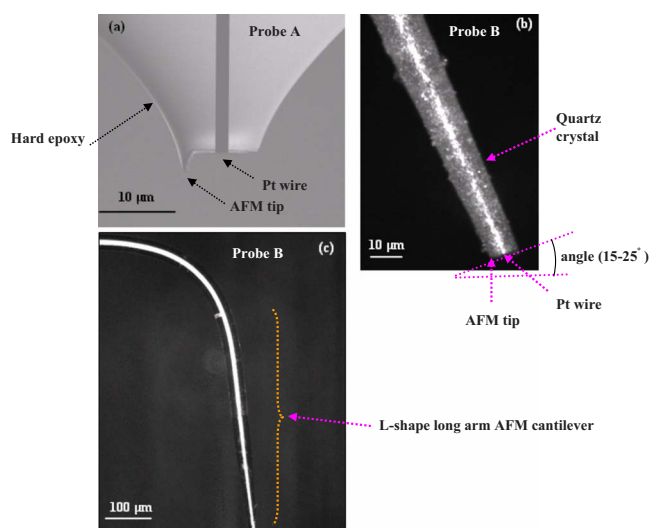
Figure 2. (Color online) Dual-mode AFM/SECM probes. (a) SEM micrograph of probe A, (b) CLSM image of probe B, and (c) long arm of probe B.

focal laser scanning microscopy (CLSM) image of probe B, respectively. Probe A was L-shaped, and its shoulder was flattened and coated with gold for laser reflection. It was made by pulling and embedding a Pt wire into a hard epoxy as insulating material approximately 10 μm in diameter at the end. The insulated end point was cut by FIB to produce a disk electrode with the core Pt electrode of 2–5 μm in diameter and a sharp epoxy tip as the AFM tip, as shown in Fig. 2a. Probe B was an approach developed to increase the resolution of SECM mapping, and also the stability and flexibility of the probe. It was made by pulling and embedding a Pt wire into the quartz glass insulating material (approximately 10 μm in diameter at the end), followed by a polishing step to expose the Pt wire and produce an inclination angle of 15–25°, as seen in Fig. 2b. With this inclination angle, one can use the end point of quartz glass as the AFM tip and the Pt wire in the middle as the SECM microelectrode. A lower angle gives a better blocking effect, whereas a higher angle gives a sharper end point for the AFM tip. In this case, it could be possible to reduce the diameter of the Pt wire to ca. 1 μm or even smaller. This has been confirmed by calculations of the measured limiting diffusion current of the microelectrode (shown later).

In contrast to other approaches to produce AFM/SECM probes,[20,21,23,25] the AFM shoulder for laser deflection in both probe A and B configurations was not immersed in the electrolyte. This was achieved through an L-shaped long bending arm (between 2 and 3 mm), as can be seen in the CSLM image of probe B in Fig. 2c. This arm geometry enables immersion of the sample surface of at least 1.5 mm in the solution without disturbing the laser reflection on the AFM shoulder.

Sample and solution for calibration.— For in situ AFM/SECM measurements of the calibration sample, a microchip with well-defined gold bands 10 μm in width and 0.5 μm in height was supplied by Windsor Scientific Ltd, U.K. The gold band sample was fixed horizontally on a base and connected to the circuit by using a silver-based conducting adhesive, and then mounted in a low-viscosity epoxy, leaving the exposed surface area facing upward.

Reagent chemicals NaCl, KCl, KI, $K_3Fe(CN)_6$, and $K_4Fe(CN)_6$, provided by Sigma-Aldrich, and distilled water were used to make up the solutions. The solutions were aerated in all the experiments. For the calibration measurements of the dual-mode probe, either I^-/I_3^- or $Fe(CN)_6^{3+}/Fe(CN)_6^{4+}$ redox couple as a mediator and KCl as supporting electrolyte were used. Regarding reactions on Pt microelectrode and gold band surfaces, the current measured on SECM tip

through the oxidation of KI or $K_3Fe(CN)_6/K_4[Fe(CN)_6]$ is due to the reactions $3I^- = I_3^- + 2e^-$ or $Fe^{++} = Fe^{+++} + e^-$, respectively.

Measurements described for gold bands have been clearly explained to illustrate the feedback mode SECM measurement which can be achieved (the potential of the Pt microelectrode and the sample was controlled at 0.6 and 0.0 V vs Ag/AgCl). This means that on gold bands the Fe^{++} are oxidized and on Pt (SECM tip) Fe^{+++} is reduced.

In this paper, to characterize the Pt microelectrode size, the best cyclic voltammetry (CV) curves obtained are given only for the KI mediator (which is less available in references) and the CV curves are not presented for the $K_3[Fe(CN)_6]/K_4[Fe(CN)_6]$ mediator (which can be found easily in the references). The aim was to verify that the Pt wire embedded in an insulating sheath acts as a microelectrode (sigmoidal CV curve) and an estimation of microelectrode size was also acquired (shown later).

Mathematical Formulation

Basic governing equations.— A 3D mass diffusion and fluid flow model has been employed for the prediction of the Pt microelectrode current during the SECM operation under steady-state and transient conditions. The following equations have been solved with appropriate boundary conditions. It is assumed that the diffusion coefficient is identical for reduced and oxidized redox species ($D_R = D_O = D$), and the total concentration of the redox species (c_R and c_O) is conserved and equal to the bulk concentration c_b, i.e., $c_b = c_R + c_O$.[30-34,39,40] Thus, the 3D concentration equation, considering momentum effects and without homogeneous reactions, is as follows

$$\frac{\partial c}{\partial t} + \mathbf{u} \times \nabla c = \nabla \times (D \nabla c) \qquad [3]$$

where c is the concentration of oxidized species (mol/L^3) c_O, D is the diffusion coefficient (L^2/T), and $\mathbf{u}$ is the velocity vector (L/T). L is length and T is time. On the left side of Eq. 3 the first term is the time dependency of concentration, and the second one is the convective term. On the right side is the diffusive term. It is also assumed that there is enough supporting electrolyte with a sufficient conductivity.

Assuming an incompressible and Newtonian liquid flow, the velocity field could be calculated by solving the generalized time-dependent continuity and Navier–Stokes momentum equations, Eq. 4 and 5, respectively

$$\frac{\partial \rho}{\partial t} + \nabla \times \mathbf{u} = 0 \qquad [4]$$

$$\rho \frac{\partial \mathbf{u}}{\partial t} - \eta \nabla^2 \mathbf{u} + \rho(\mathbf{u} \times \nabla \mathbf{u}) + \nabla p = 0 \qquad [5]$$

In Eq. 4 and 5, η is the dynamic viscosity (M/LT), ρ is the density (M/L^3), and p is the pressure (M/LT^2), where M is the mass.

To compare the results of Eq. 3 with that of nonconvective conditions, the following equation is considered

$$\frac{\partial c}{\partial t} - \nabla \times (D \nabla c) = 0 \qquad [6]$$

Boundary conditions.— A 3D Cartesian coordinate system is used in the calculation, while only half of the work piece is considered because the problem is symmetrical in the *y*-axis. Figures 3a and b show schematic plots of the boundary domain/conditions and geometrical model of probes A and B, respectively. To simplify the visual appearance, only insulating parts of the boundary domain were highlighted in these figures. We have used the general terms and concepts to define the boundary conditions that have been used in the other references such as inlet and outlet, insulating, slip, and no-slip boundary conditions.[28-34,39,40] Therefore, the results on simu-
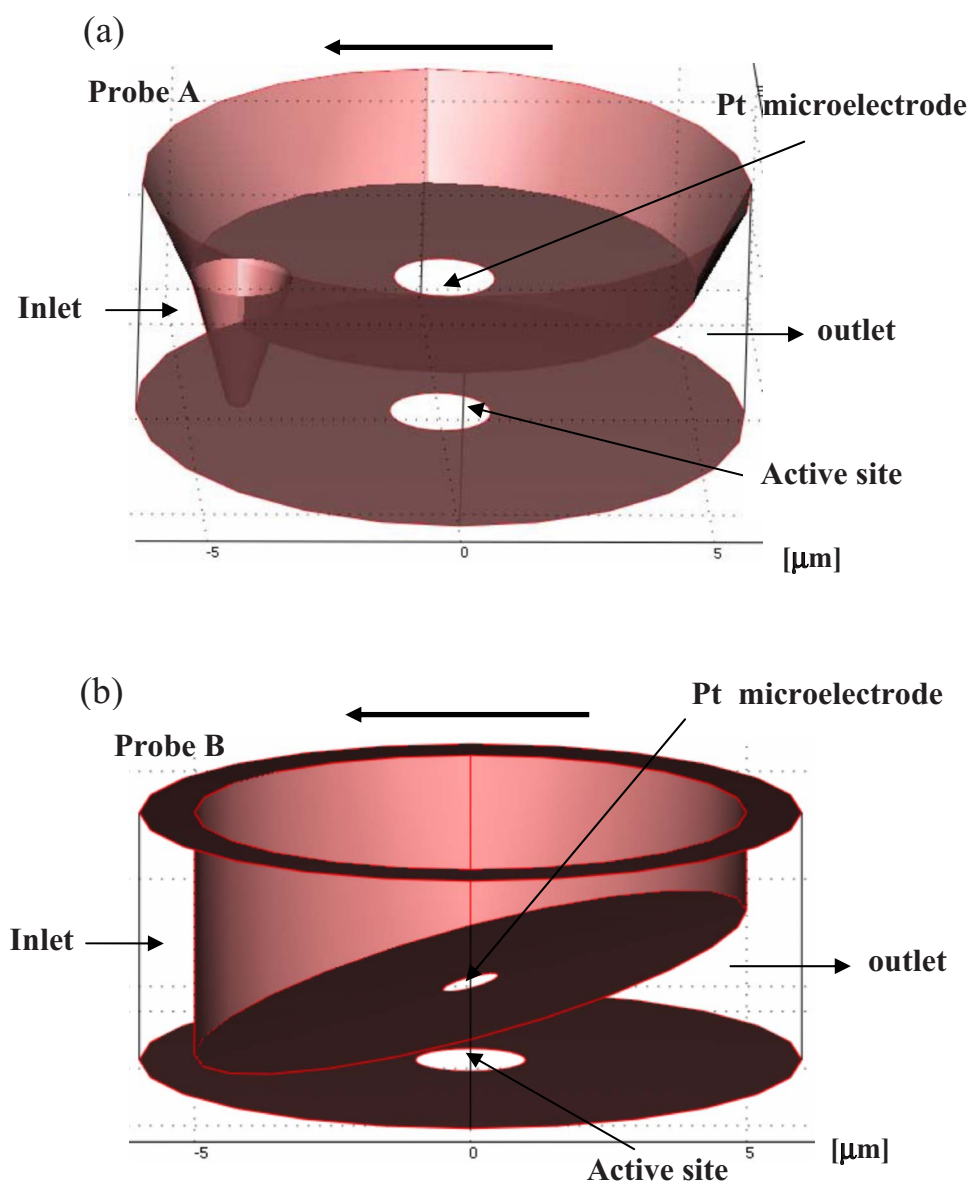
Figure 3. (Color online) SECM simulation boundary domain of (a) probe A and (b) probe B. The thick arrows show the scan direction.

lation can be reproduced by the others using the same boundary conditions that we have employed. In summary, the boundary conditions are presented below.[28-34,39,40]

For the diffusion-convection mass transport Eq. 3

1. $c = 0$ at inlet, outlet, and active site on the sample surface,
2. $c = c_b$ at Pt electrode surface,
3. $n \times \nabla c = 0$ at insulating parts of substrate and tip, and symmetric plane of half of the probe in the y direction; n is the unit vector in x, y, and z directions.

For the momentum Navier–Stokes equation, Eq. 5

1. $\mathbf{u} = 0$, no slip (zero velocity) at the sample surface,
2. $\mathbf{u} = (U,0,0)$, slip (constant velocity) at probe surface, where U is the probe velocity as a function of scan rate (Hz), in one (x) direction.
3. $\nabla^2 u = 0$ at inlet and outlet,
4. $n \times \mathbf{u} = 0$, slip in symmetry boundary.

Numerical simulation.— Finding the optimal size for considering the bulk solution and shape of a modeling domain is always a trade-off between numerical accuracy and model validity. The modeling domain should be as large as possible to minimize the influence of bulk concentration on the calculation. However, making the geometry too large decreases the speed of computation and may not resolve the details well. Because our interest was focused on the behavior of the solution and the effect of velocity on the Pt-electrode current collection, the boundary domain was truncated to the region displayed in Fig. 3 for probes A and B. The results for a few different meshes and domain sizes were compared. It was found that there is a point where the gain in accuracy from further increasing the domain size is outweighed by the loss from using a coarser mesh for a given number of degrees of freedom. To obtain an optimal mesh number, we applied nonuniform elements for maximum resolution of variables. The mesh was relatively coarse in the bulk boundaries, whereas much finer elements were used on the Pt electrode and active sites.

An optimum mesh number was obtained such that from that point reducing the mesh size would not improve the numerical solution accuracy compared to analytical data from a limiting current formula $(i_\infty = 4nFDca)$.[39,40] Based on that result, a maximum element size of 0.1 μm was chosen for the simulation.

All simulations were carried out in actual dimensions with rel-

Table I. Physical properties used as input in SECM simulations.

Physical properties	Value
Diffusion coefficient, D (m²/s)	8×10^{-10}
Density of liquid, ρ (kg/m³)	1000
Viscosity of liquid, η (kg/m s)	0.0015
Concentration of bulk, c_b (M)	0.005
Probe velocity, U (μm/s)	22–704

evant parameters. The Pt microelectrode diameter was assumed to be 2 μm for probe A and 1 μm for probe B, except in some simulations where 2 μm was used for both the probes to investigate the influence of a certain parameter. As shown in Fig. 3, an active site of 1 to 2 μm diameter on the sample surface was considered as a local corroding site. A distance of 100 nm was chosen as the gap between the sample surface and the AFM tip to simulate a 100 nm lift-up distance, which has been commonly used during the AFM/SECM measurements. To avoid any discontinuity in the simulation and also consider a real shape of probe A, a semispherical shape with a radius of 250 nm was added to the end of the AFM tip, as can be seen in Fig. 3a. This enables the simulation to be run without any singularity problem.

The total current, i_T, on the Pt electrode surface was calculated by an integration of the concentration gradient, ($\partial c/\partial n$); here, n is the unit vector in the x, y, and z directions, as follows

$$i_T = nFD \int_A \frac{\partial c}{\partial n} ds \qquad [7]$$

where F is the Faraday constant, the constant n is the number of electrons transferred, A is the surface area of the Pt microelectrode, and ds is the incremental electrode surface area. The physical properties and work piece information, i.e., the input data employed in the calculation of fluid flow and mass diffusion, are summarized in Table I.

The D, ρ, and η values were taken from the available literature.[33,38,39] The bulk redox concentration of 0.005 M and the probe velocity range (corresponding to a scan rate range 0.25–8 Hz) were normally used in the experiments.

To numerically solve the governing equations, commercial finite element-based software Comsol 3.3 (Comsol Ltd.) was used in this work.

Results and Discussion

The results are presented in the following simulation and experimental sections, including instrument and Pt microelectrode characterization and calibration. Meanwhile, comparisons between the results obtained in two parts are given during the discussion.

The numerical simulation can be divided into two categories, static and dynamic. One interesting topic in the SECM simulation is to numerically estimate the static approaching curve when the probe moves from the bulk solution to the vicinity of the sample surface.[28,30-32,39,40] As an example in corrosion studies, the probe reaction is investigated when it reaches either active sites (local corroding points) or a passive area (semi-insulating region). This condition can be categorized as static SECM simulation. The surface with local corroding sites can be scanned by the SECM and the local electrochemical activities could be imaged. This situation can be categorized as dynamic SECM simulation.[28,33] For the SECM mapping, the resolution of SECM is an important issue because it determines how the small size of local active sites can be resolved and how the small distance between active sites can be distinguished. The SECM resolution can be evaluated in temporal (time) and spatial (lateral) domains, which are discussed in the following sections.

Simulation results.— Dynamic simulation, effect of convection.— During SCEM scanning, the dynamic situation of the fluid may have an influence on the ionic transport, i.e., a convective term
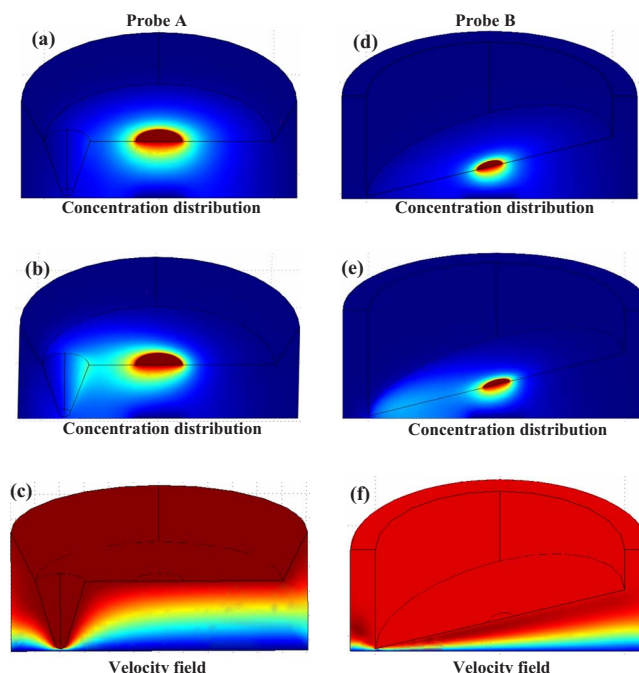

Figure 4. (Color online) (a), (b), (d), (e) Concentration distribution and (c), (f) velocity field in the boundary domain for probe A (a)–(c) and probe B (d)–(f) obtained from (a), (d) diffusion Eq. 6, (b), (e) diffusion–convection, Eq. 4, and (c), (f) momentum Eq. 4 and 5. Velocity field from $u = 0$ to $u = u_{max}$ and concentration profile from $c = 0$ to $c = c_{max}$. The probe scan rate is zero in (a) and (d) and is 8 Hz in (b), (c) and (e), (f).

in addition to diffusion. To estimate the influence of convective contribution on total ionic transport of the mediator, Eq. 3-5 were numerically solved. As an example, Fig. 4 shows concentration profiles obtained under the diffusive condition and diffusive–convective condition with a scan rate of 8 Hz (probe velocity 704 μm/s), and the velocity field for probes A and B, respectively. This scan rate may be necessary in fast reaction rate studies like localized corrosion, where pitting and prepitting events on the micrometer scale could occur with fast kinetics. This gives opportunities to image those local events occurring on the surface. Comparing Fig. 4a and b and Fig. 4d and e reveals the convection influence on the concentration profile, which is more pronounced for probe A.

The convection term also causes an increase in the total current on the Pt microelectrode (calculated by Eq. 7). In addition, due to the asymmetric shape of the probes, the velocity field is deviated around the AFM end point. In summary, the deviation from pure diffusive transport strongly depends on the scan rate (probe velocity).

Figure 5a shows the fraction of convective current that can be collected by the Pt microelectrode as a function of the scan rate. According to the results, the fraction of convective current for probe B increases almost linearly with the scan rate, and is generally higher than that for probe A. This can be explained by a shorter distance between the Pt microelectrode and sample surface for probe B. For a limit of convective effect of 2%, probe A can be used with a scan rate of up to ca. 4 Hz, in contrast to below 2 Hz for probe B. For both probes A and B with the scan rate normally used (0.25–2 Hz), the diffusive part is predominant in the SECM current collection, and the convective contribution is about 2% or less and can be neglected, which is in agreement with the literature.[34] Hence, during the normal scan rate, diffusion Eq. 6 can be implemented with appropriate accuracy. A fast scan rate may be desirable when using the SECM for monitoring the transient events involved, for instance, fast kinetic-like localized corrosion. According to the results, if the
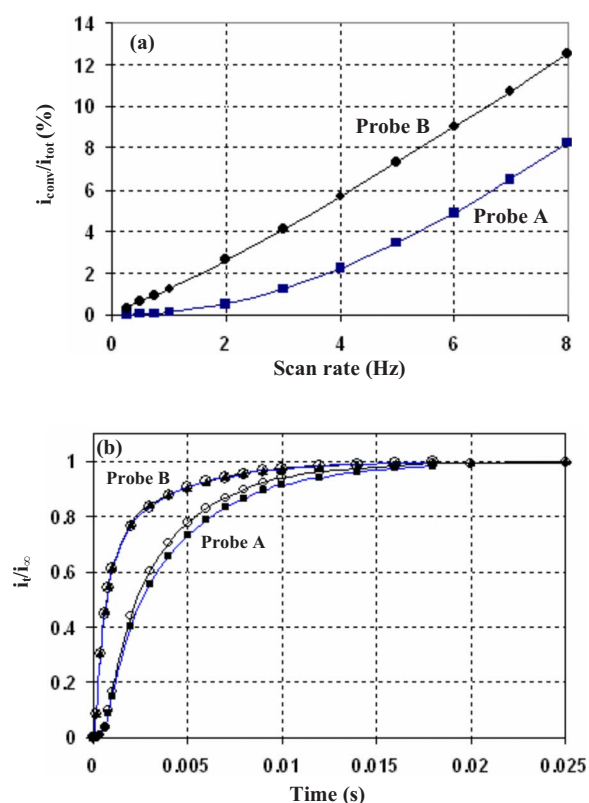
Figure 5. (Color online) (a) Percentage of convective term (i_{conv}) of total current (i_{tot}, diffusion and convection) for probes A and B, respectively and (b) relative current (i_t/i_∞) vs time, showing the time needed to reach the steady-state diffusion condition for probes A and B, for diffusion only (filled symbols) and diffusion plus convection (open symbols).

Figure 6. Scaled current (i_t/i_{max}) for probes A and B (Pt diameter 2 μm) during scanning of the active site 2 μm in diameter shown schematically in Fig. 3.

probe scans the surface with a scan rate higher than 4 Hz, the convective effect on the SECM current imaging should be considered in the interpretation.[34]

Temporal resolution.— In a static simulation, the time-dependent diffusion–convection and diffusion equations, Eq. 3 and 6, have been solved to find the time required to reach steady-state conditions (time-independent) for estimation of the temporal resolution. Figure 5b shows the time needed to reach the steady-state condition for probes A and B, respectively, with a scan rate of 8 Hz, with respect to diffusion only and diffusion–convection conditions. It is estimated for probe A that within ca. 0.005 s the current reaches 80% of the steady-state value, whereas for probe B the corresponding time is less than 0.002 s because of a smaller distance between the Pt microelectrode and sample surface. In practice, with normal SECM data acquisition, the probe stays at each point for a few milliseconds. As an example, with a scan rate of 1 Hz and 256 × 256 pixel data sampling, the corresponding time at each point is ca. 0.004 s. This implies that the collected current is close to that at the steady-state conditions.

Clearly, the sample–electrode distance, a geometrical parameter, has a strong influence on the temporal resolution. It was also observed that the time required to reach steady state strongly depends on the electrochemical parameters, particularly the diffusion coefficient of the redox species. This indicates the importance of providing enough supporting electrolyte to facilitate the ionic transport in the boundary domain. Moreover, as shown in Fig. 5b, for probe A with a scan rate of 8 Hz (fast scan), the convection slightly decreases the time needed to reach the steady state. This effect is not observed for probe B (no difference between diffusion only and diffusion–convection conditions), which is due to a smaller distance between the Pt microelectrode and the sample surface.
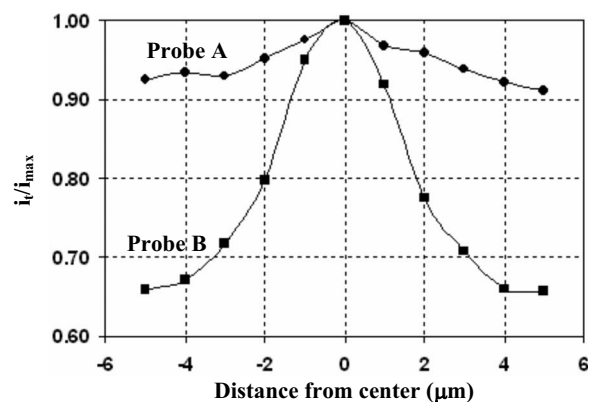
In summary, the calculations on temporal resolution clarify that, for this particular geometrical configuration of probes A and B, the SECM data acquisition performs under or close to the steady-state conditions for both probes A and B.[39,40]

Spatial resolution.— In addition to the influence of electrochemical parameters such as the diffusion coefficient, electrochemical reaction kinetics, etc., the spatial resolution for the SECM current collection also depends on geometrical parameters. In this section, the effects of geometrical parameters were simulated and the results for probes A and B are compared and discussed below.

Scanning over one active site.— Dynamic simulation of SECM scanning over an active site was reported using the BEM.[28] To estimate the spatial resolution of probes A and B, the simulation was run on the surface with one active site, as schematically shown in Fig. 3. For this purpose, the active site was entered into the computation domain from the left side, moved through the whole region, and then left the computation domain from the right side. Figure 6 shows the scaled current (with maximum current related to the active site in the center) for probes A and B. In this case, the Pt microelectrodes in both probes and the active site were 2 μm in diameter. As can be seen, both probes show a maximum current in the middle when the active site is located exactly below the Pt microelectrode. When the probe was moved away from the position of the active site, the current decreased sharply with probe B but more slowly with probe A, indicating a better blocking effect of probe B. With respect to the lateral resolution, one can see that the enhanced current was collected over an area larger than the active site. For probe B under the simulated conditions, the size with 95% of maximum current is about the same as the active site, while the size with 80% of maximum current is approximately two times larger than that of the active site.

The asymmetric geometry of the probe, i.e., the AFM tip on one side of probe A and an inclined end point of probe B, causes some nonsymmetrical results. For probe A the AFM tip acts as a diffusion barrier, while for probe B the inclined surface has a shielding effect. This effect is also reflected in Fig. 6, where the current profiles are not exactly symmetric, which is more pronounced for probe B than for probe A. The current at the same distance from the center is higher at the left side than at the right side.

A microchip gold band 10 μm in width embedded in 10 μm insulating material has been used for calibration purposes in a later section. To resemble these situations, the simulations were carried out for two cases where the whole surface was completely insulated or acted as an active site. The results showed that in probe A, the Pt current ratio (insulating/active) is around 85%, while for probe B, a current ratio around 75% is obtained.

Influence of distance between two active sites.— Static simulation of SECM current collection was performed to study the influence of
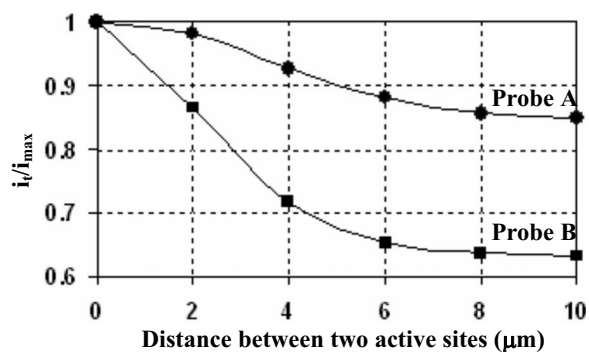
Figure 7. Relative current (i_t/i_{max}) of probes A and B vs the distance between two active sites 2 μm in diameter.

distance between actives sites. Here, the probe position was fixed in the center between two active sites. Figure 7 shows the effect of separation distance between two actives sites 2 μm in diameter, in terms of the scaled current of the Pt microelectrode for probes A and B. The Pt microelectrode in both probes was 2 μm in diameter, and two active sites with the separation distance 0, 2, 4, 8, and 10 μm from each other were considered in the simulation. The calculated current values were scaled to the maximum value obtained when the two active sites were at a distance of zero from each other. The scaled current decreases with increasing separation distance, more rapidly for probe B, with a scaled current of 0.63 for probe B and 0.87 for probe A at a separation distance of 10 μm between the active sites. The more rapid drop for probe B is explained by its better blocking effect. Beyond a certain separation distance, approximately 6 μm for probe B and 8 μm for probe A, the current level reaches the level corresponding to infinite distance between two active sites.

Scanning over two active sites.— Following the procedure reported,[33] a sequence of dynamic simulations was performed where the probe scanned the surface over two active sites 1 μm in diameter, with a separation distance of 2 and 4 μm, respectively, as schematically shown in Fig. 8a. Here, the Pt microelectrode diameter was 2 μm for probe A and 1 μm for probe B, respectively, i.e., similar to the actual probe dimensions. In this case, the maximum current was obtained on the active site (point 1) at the left side, and the rest of the current values were scaled relative to this point. Figure 8b shows the scaled current as the function of probe position for the two active sites with a separation distance of 4 μm. The center (point 2) is defined as the middle point between the two active sites and point 3 corresponds to the active site at the right side. With probe B, two current peaks could be resolved during scanning because of an approximately 7% current drop in the current in the middle of the two active sites. With probe A, the current in the middle region was only 2% lower than the peak current, with difficulties resolving the two active sites. However, if the separation distance between the two active sites decreased to 2 μm, they could not be resolved even with probe B (see Fig. 8c), and only a plateau of enhanced current was observed.

In all, the results suggest a higher lateral resolution for probe B than probe A, and, with these geometrical configurations, approximately a 3–4 μm separation distance is needed for active sites of 1 μm in size to be resolved by SECM mapping using probe B.

Moreover, the asymmetric effect can also be seen in current values when comparing the left and right sides, Fig. 8b and c. Due to a better blocking effect, the left side shows a slightly higher current compared to the right one for both probes A and B.

Influence of neighboring active sites on probe current.— Based on the results from the static simulation of the situations schematically shown in Fig. 9, the current contribution to the Pt microelectrode from two neighboring active sites can be calculated. Here, the fraction of current was calculated from an active site beneath the Pt
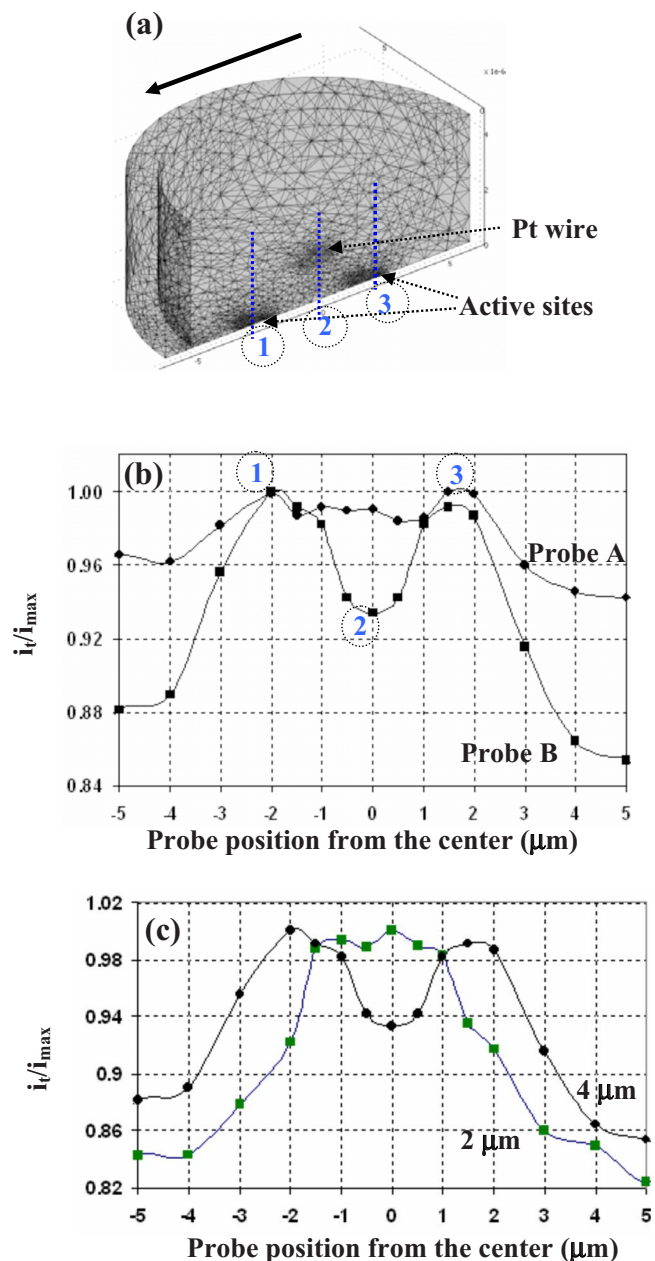
Figure 8. (Color online) (a) Mesh used for simulation of current for probes during scanning of two active sites 1 μm in diameter, (b) scaled current (i_t/i_{max}) on probe A (circle) and B (square) with 4 μm distance vs probe position from the center and corresponding points 1, 2, and 3 labeled in (a), and (c) scaled current (i_t/i_{max}) on probe B with 2 and 4 μm distance, respectively. Pt microelectrode diameter in probe A is 2 μm and in probe B is 1 μm.

microelectrode in the center and from another active site located 2 μm away from the center. With probe A, 34% of the total current from the two active sites will contribute to the current collected by the Pt microelectrode, and the rest will spread out to the bulk. The fraction of the collected current from the active site in the center is 79%, and from another active site 2 μm away from the center about 21%. In contrast, with probe B, 64% of the total current from two active sites would be collected by the Pt microelectrode. The fraction from the active site in the center is 90% and from another active site, at distance of 2 μm, is about 10%. This confirms that probe B
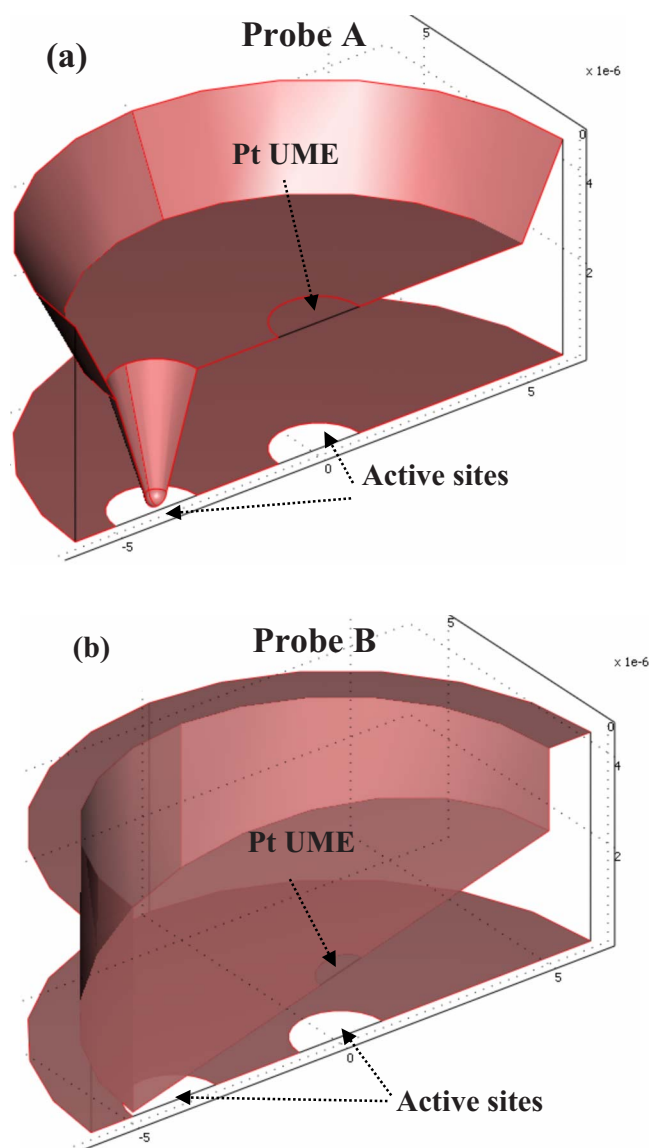
Figure 9. (Color online) Schematic pictures for calculation of fraction of current collection from an active site beneath the Pt microelectrode in the center, and an active site located 2 μm from the center, for (a) probe A and (b) B, respectively.

Figure 10. (Color online) (a) SECM calibration using a 1 GΩ resistance as dummy cell and applying −1 to 1 V potential, scan rate 100 mV/s. (b) Noise measurement for Faraday's cage efficiency, current noise ∼20 pA.

gives a better blocking effect (less contribution from bulk) and a higher spatial resolution (less influence from the neighboring active site).

Influence of sample–electrode distance.— Comparing probes A and B, the effect of sample–electrode distance can be seen from the convective influence (Fig. 4), steady-state and transient currents (Fig. 5), and the current distribution during scanning over one (Fig. 6) and two active sites (Fig. 8). Clearly, reducing the sample–electrode distance results in a higher lateral resolution. Moreover, for the probes shown in Fig. 3, it is calculated that probe A with a Pt microelectrode 2 μm in diameter and a sample–electrode distance of 2.85 μm collects 52% of the total current, whereas probe B with the same Pt microelectrode size and sample–electrode distance around 1 μm collects 60% of the total current. All these results confirm that this probe design gives better temporal and spatial resolutions.

Influence of Pt microelectrode diameter.— Generally, reducing the diameter of the Pt microelectrode favors achieving higher resolution SECM measurements.[39,40] For probe B, it was possible to reduce the
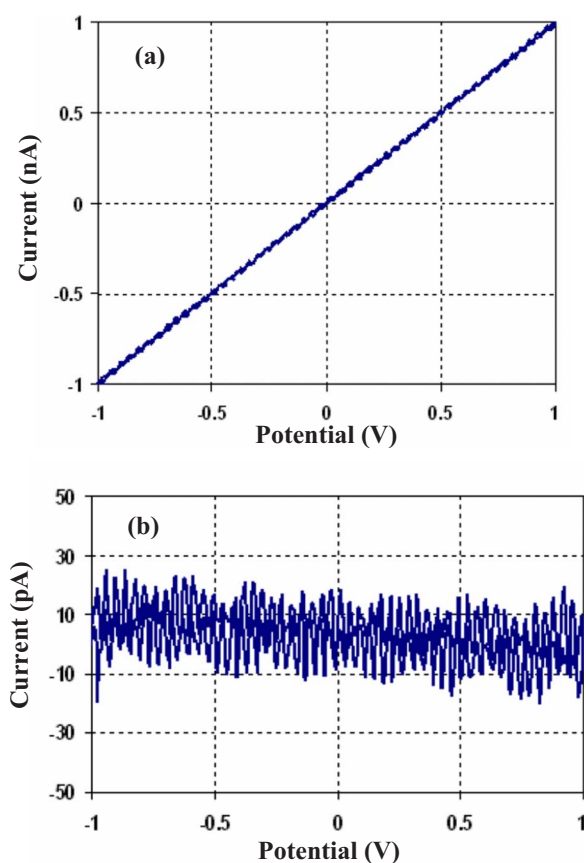
Pt microelectrode diameter down to 1 μm, and as shown in Fig. 8c, this smaller size gives a better lateral resolution. The geometrical configuration of probe B also decreases the sample–electrode distance to ca. 1 μm, which is also helpful for achieving higher resolution. However, due to the inclination angle, the asymmetric effect on current collection at the Pt microelectrode in probe B is more pronounced. Decreasing this angle gives a better blocking effect and a smaller sample–electrode distance, which in turn provides a higher resolution possibility for the SECM part, but it may reduce the AFM spatial resolution because the end point of the probe is not sharp. This could be an issue to simulate the SECM and find out the influence of inclination angle on both AFM resolution and SECM asymmetric effect.

All simulations for the resolution studies were carried out by the assumption that the convection term is negligible. However, the contribution of both convection and diffusion terms in the resolution of SECM, as shown in Fig. 5, indicates that a particularly fast scan rate would be of interest. Note that all the simulations were performed for one scan direction (x axis), as shown schematically in Fig. 3. Because of the asymmetric geometry of the probes, the influence of scan direction on the SECM resolution and current distribution is of interest to study.

Instrument noise level.— Figure 10a shows the voltammetric response of a dummy cell containing a precise resistor of 1 GΩ when the potential was swept from −1 to 1 V with a scan rate of 100 mV/s. As expected from Ohm's law ($I = V/R$), the current response from −1 to 1 nA and a linear relationship with slope 1 were observed, and deviation from the coordinate center was negligible at the nA scale; see Fig. 10a. To evaluate the error level for the current measurement in the picoscale range, the current noise was obtained
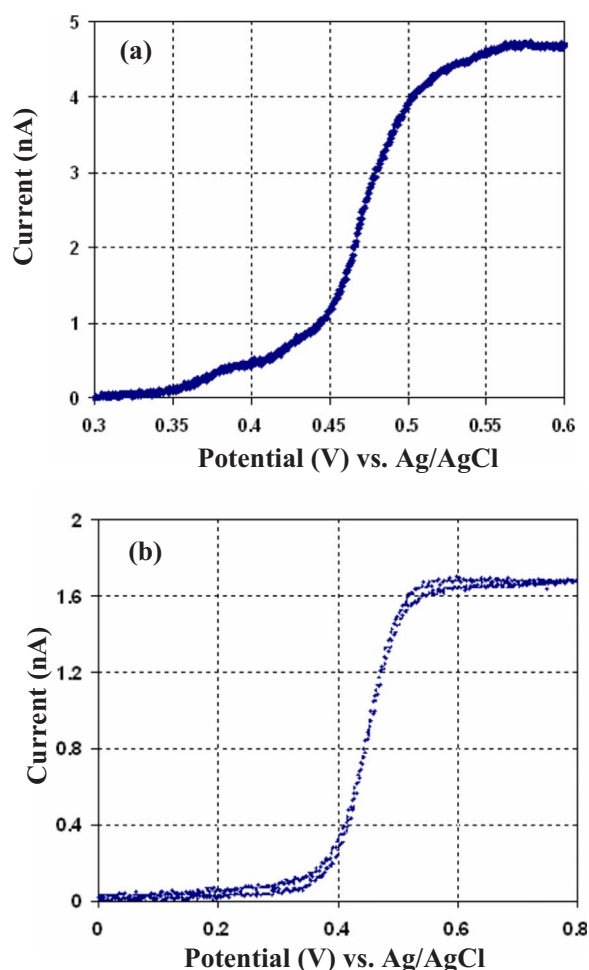
Figure 12. (Color online) (a) AFM image of microchip gold band calibration sample in air, using contact mode Si-based AFM tip, and (b) line profile of an individual gold band. Scan rate 1 Hz.

Figure 11. (Color online) (a) CV characterization of probe A. Using KI as mediator, the actual probe size was in the range of 2 μm in 20 mM KI. (b) CV characterization of probe B. Using KI as mediator, the actual probe size was in the range of 1 μm in 5 mM KI. In both cases, sufficient NaCl was used as supporting electrolyte. Scan rate was 100 mV/s.

by deducing the calculated ohmic current from the measured current values, and the results are displayed in Fig. 10b. The noise level of the instrument was thus estimated to be around 20 pA. The current noise may originate from the instrumentation or environment stray current. This error could be also an indication of the grounding system and Faraday cage efficiency. This implies that, when measuring current in the nA range or above, the error of data acquisition by the instrument is acceptable, whereas when the current is at the pA level, the noise influence should be taken into account.

CV characterization of the Pt microelectrode.— The Pt microelectrode in the probe may in reality not have a perfect disk shape, and thus may deviate from the analytical formulation in the modeling work. Moreover, the actually exposed size of the Pt microelectrode may vary due to contamination in the solution. Therefore, the real active surface area of the Pt microelectrode cannot be determined from normal microscopic images such as shown in Fig. 2. Instead, CV was used herein for probe characterization and size evaluation. In the ideal situation, it has been proven that the CV for a microelectrode should appear in a sigmoidal shape.[39,40] Besides, CV cycling may act as a cleaning process, because hydrogen evolution on the Pt microelectrode could help to remove contaminants from the surface. In this work, CV measurements were performed before any calibration was performed.

Figures 11a and b show CV curves for probes A and B, respectively, with KI as the mediator and a scan rate of 100 mV/s. Based
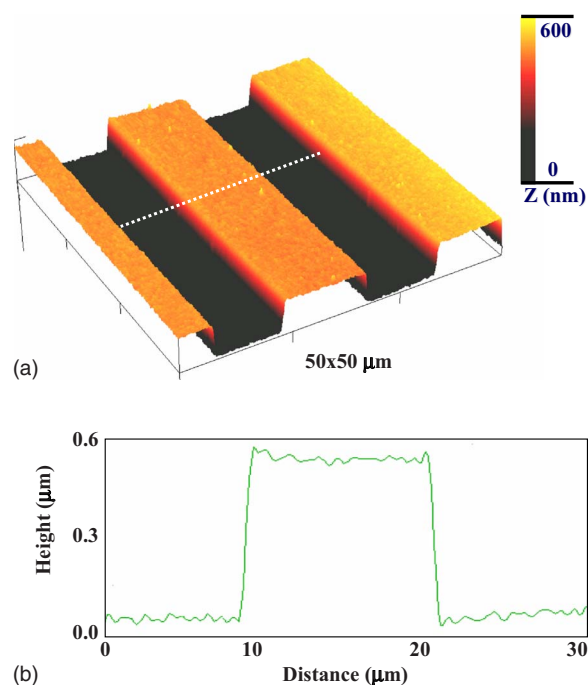
on the results, the microelectrode potential during the AFM/SECM experiment was controlled in the range of limiting current, e.g., 600 mV vs Ag/AgCl. In addition, the radius of the microelectrode could be estimated from the limiting current formula for a planar disk electrode[32,33,39,40]

$$i_\infty = nFDca \qquad [8]$$

where i_∞ is the limiting current, n is the number of electron transfer by mediator, F is the Faraday constant, D is the diffusivity coefficient, c is the concentration of mediator, and a is the Pt microelectrode radius. Assuming $D = 8 \times 10^{-6}$ m^2/s and taking the limiting current from the CV curves, Fig. 11, 5 nA for probe A in 20 mM KI and 1.6 nA for probe B in 5 mM KI, the Pt electrode radius for probes A and B is estimated to be approximately 1 and 0.5 μm, respectively, i.e., the diameter equal to 2 and 1 μm, respectively.

Calibration of integrated AFM/SECM.— Different calibration samples such as highly oriented pyrolytic graphite, gold mesh, microchip gold band, and Pt microband have been used for AFM/SECM calibration measurements.[13-24] In the present study, a microchip gold band was used for calibration of the AFM/SECM probes. The microchip gold bands were inserted in an insulating substrate. Some of these microbands were connected to the circuit using silver glue, and the glue part was covered by a lacquer, which provides ideal active/insulated regions with a well-defined interface on the surface. The gold band dimensions were imaged first in the air by normal AFM scanning of the surface using a standard Si-based AFM tip in contact mode. Figure 12 shows a 3D topography image (Fig. 13a) and a height profile (Fig. 13b) of the gold band calibration sample. As can be seen from the line profile, the width and height of the individual gold band were very close to the nominal dimensions (10 and 0.5 μm, respectively). Besides, the roughness is estimated to be approximately 50 nm. Despite a slight edge effect at both sides of the gold band due to artifacts from the AFM tip convolution, a sharp edge can be seen between the gold band and the insulating region.

Probe A.— Concurrent topography and electrochemical current mapping was performed on the microchip gold band sample, using
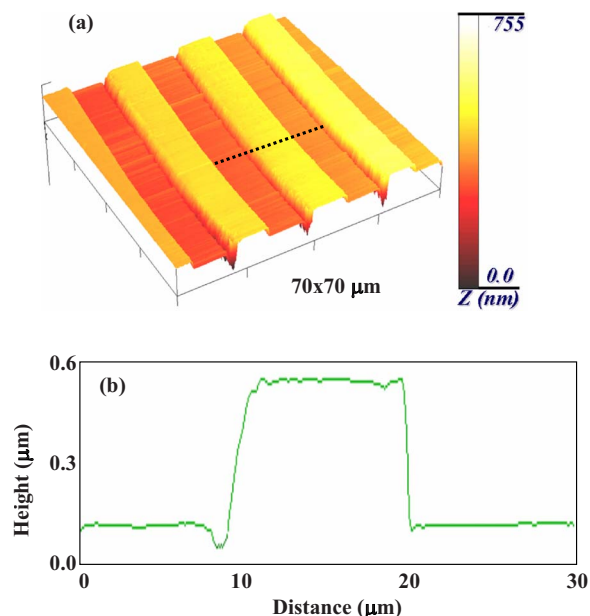
Figure 13. (Color online) (a) In situ AFM image (concurrent with SECM image in Fig. 14a) of gold band in 0.5 M KCl and 20 mM $Fe(CN)_6^{3+}/Fe(CN)_6^{4+}$ using probe A, and (b) line profile of an individual gold band. The Pt microelectrode potential and substrate potential 0.6 and 0 V, respectively, vs Ag/AgCl reference electrode, Pt microelectrode size ca. 2 μm. Scan rate 1 Hz.

probe A in 0.5 M KCl solution containing 20 mM $K_3[Fe(CN)_6]/K_4[Fe(CN)_6]$ as the mediator. The potential of the Pt microelectrode and the sample was controlled at 0.6 and 0.0 V (usually used for gold band calibration sample) vs Ag/AgCl, respectively, and the scan rate was 1 Hz. Figures 13 and 14 show the concurrent AFM and SECM images obtained simultaneously. The
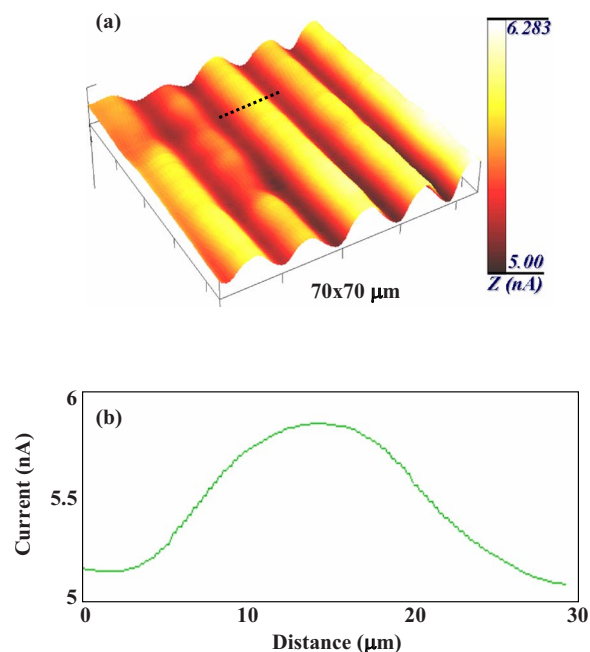

Figure 14. (Color online) (a) SECM image (concurrent with AFM image in Fig. 13a) on gold band in 0.5 M KCl and 20 mM $Fe(CN)_6^{3+}/Fe(CN)_6^{4+}$ using probe A, and (b) line profile of electrochemical current on an individual active gold band. The experimental conditions are the same as in Fig. 13.

gold bands were clearly seen in the topography image in Fig. 13a. From the line profile of an individual gold band shown in Fig. 13b, the width and height of the band were also close to the nominal dimensions. The surface appeared quite flat on a micrometer scale, probably because the AFM tip of probe A was not sharp enough to detect the roughness on a nanometer scale. Besides, an edge artifact, an overshot drop about 200 nm in depth, is evident at the left side of the gold band. This artifact may be due to an asymmetrical geometry of probe A and influence of the scan direction on the image. Nevertheless, from the resolution point of view, it can be concluded that the dual-mode probe A is able to follow the topography feature on a micrometer scale with an acceptable accuracy similar to the results reported previously.[23,24]

The SECM image in Fig. 14 shows the electrochemical current variations on the gold bands. In general, the gold bands exhibited enhanced current, Fig. 14a, and the difference in current between the maximum and the minimum values is about 1.3 nA, so the noise influence is negligible. The distance between points having the maximum and minimum current is about 10 μm, the same as the width of the gold bands. A lower current at some points was also observed on the gold band, probably due to contamination. In contrast to the concurrent AFM image, the SECM image does not show a sharp edge due to the spreading of the current to neighboring volume. This has to be taken into account in the interpretation of the SECM images. Figure 14b presents a current line profile of an individual active band, showing that the current is at maximum in the middle of the active band and decreases slowly toward the edge of the band to a minimum value. This is in agreement with the numeric simulation in which the current peak is predicted to appear in the middle when the probe scans over one active site, Fig. 6. Furthermore, the slight asymmetric distribution of the current at the two sides of the gold band is also evident in Fig. 14b, in accordance with the simulation results in Fig. 6 and 8. Here, instead of one active site 1–2 μm in size, the active gold band is about 10 μm in width. According to the simulation for scanning a conductive area and an insulting area of 10 μm diameter each, the ratio of the current values between the insulating area and the conductive area is around 85%. Judged from the Z-scale in Fig. 14a, the ratio between the minimum current on the insulating region and the maximum current on the gold band is approximately 80%, in good agreement with the simulation results in a previous section.

Probe B.— Calibration measurements were also performed using probe B on another calibration sample. In this case, the solution was 0.5 M KCl containing 5 mM $K_3[Fe(CN)_6]/K_4[Fe(CN)_6]$. This lower mediator concentration (as compared to above) was found to be satisfactory based on the CV response of probe B (Fig. 11b). The concurrent AFM and SECM images are shown in Fig. 15 and 16, respectively. Compared to probe A in Fig. 13 and 14, it seems that, although probe B is able to follow the general topography features, the quality of the topography image (Fig. 15a) is not as good as that obtained by using the standard AFM probe (Fig. 12a) or the dual-mode probe A (Fig. 13a). The AFM line profile in Fig. 15b of the gold band shows a broad edge at both sides of the band, and the height (around 0.4 μm) is slightly smaller than the nominal value (0.5 μm). This is probably due to a small inclination angle of probe B having a cross-section diameter of around 10 μm, so that the end point of the probe cannot follow the sharp edge of the sample down to a deep valley. Thus, probe B has more difficulties than probe A when scanning sharp edges. Because of the geometrical configuration, the AFM performance of probe B is lower than that of probe A. However, in real SECM applications, for instance in corrosion studies, the ability to follow such sharp edges may not be so important.

The SECM image in Fig. 16 shows the electrochemical current variations on the gold band obtained by using probe B. In this case, one of the gold bands in the scanned area seems to be activated while the other ones are not. Compared to the SECM image in Fig. 14a, the total current level is lower for probe B (Fig. 16a). This is due to the smaller size of the Pt microelectrode of probe B, and also because of a lower mediator concentration used. Judged from the
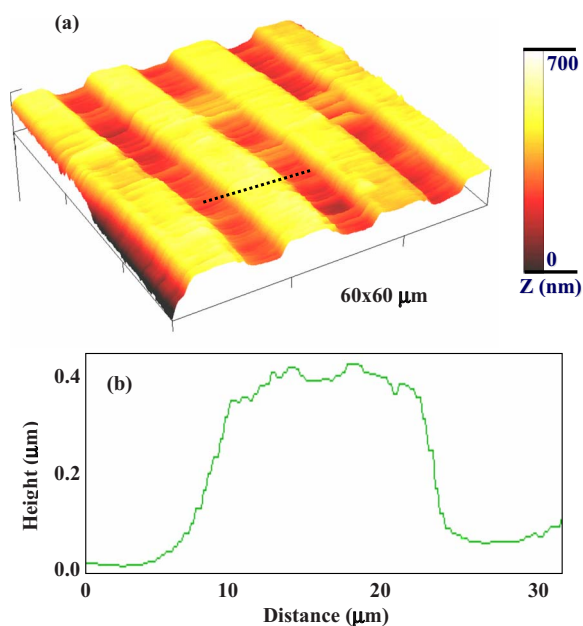
Figure 15. (Color online) (a) In situ AFM image (concurrent with SECM image in Fig. 16) of gold band in 0.5 M KCl and 5 mM $Fe(CN)_6^{3+}$/$Fe(CN)_6^{4+}$ using probe B, and (b) line profile for height variations of an individual gold band. The Pt microelectrode potential and substrate potential 0.6 and 0 V, respectively, vs Ag/AgCl reference electrode. Pt microelectrode size ca. 1 μm. Scan rate 1 Hz.

Z-scale, the difference in current between the maximum and the minimum values is about 310 pA, still far beyond the noise level. Figure 16b presents the current line profile on the active gold band, showing that the current is at maximum in the middle and decreases slowly toward the edge of the band to a minimum value. The ratio between the minimum current of the insulating region and the maximum current of the gold band is approximately 87%. Moreover, a
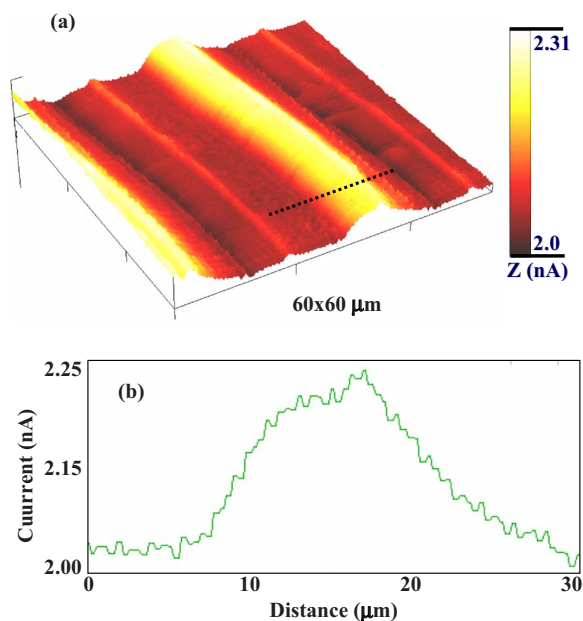

Figure 16. (Color online) (a) SECM image (concurrent with AFM image in Fig. 15a) of gold band in 0.5 M KCl and 5 mM $Fe(CN)_6^{3+}$/$Fe(CN)_6^{4+}$ using probe B, and (b) line profile for the electrochemical current on an individual active gold band. The experimental conditions are the same as in Fig. 15.

slight asymmetric distribution of the current at the two sides of the gold band is also evident. Similar to probe A, these observations are in agreement with the numeric simulations in Fig. 6. Because the total current difference is about 310 pA, and the instrument noise level is about 20 pA, the current noise is clearly seen in the line profile. This means that, to work in the pA range, the current noise level of the instrument needs to be further reduced. The results also give an indication of the minimum mediator concentration needed for the SECM measurements.

The results in the simulation results section suggested that probe B has a better lateral resolution when scanning over small active sites of a few micrometers in size as shown in Fig. 6 and 8. However, based on experimental results on the calibration sample used here, due to the large width (10 μm) of the gold band, it is difficult to distinguish any clear difference in lateral resolution between the two probes for SECM mapping. Therefore, a microchip gold band less than 2–3 μm in width would be a more suitable calibration sample to evaluate and distinguish the lateral resolution for the dual-mode probes investigated and to compare with the simulation results.

As mentioned before, the AFM-SECM combining technique has already been introduced (extensive researches during the last few years by two well-recognized groups, Macpherson et al.[13-19] and Kranz,[20-22] and also more recently by other groups[23-25]). The critical point right now on AFM-SECM combining is to find out the best way to produce a dual-mode tip probe acting as an AFM tip and SECM microelectrode. Because this is still a challenging issue, in this paper a setup of a dual-mode probe producing in a smart way has been introduced. It is state-of-art and the authors' attempt was to be specific and explain an approach to make the AFM-SECM probes, probes A and B, and to characterize them rather than speaking in broad terms. The results showed a better AFM topography image quality for probe A and a higher resolution SECM current image for probe B. This means that the latest effort to construct the AFM-SECM probe, probe B, is not optimum yet. Therefore, both designing and producing an AFM-SECM tip probe with an optimal geometry is still a demanding subject and more work is needed to be done in the future, both simulation and experimental work. However, at this stage, the quality of the results that have been obtained, particularly on SECM resolution (even the results obtained on not fully optimized calibration sample), is appreciated.

Concerning the validity of numerical simulation, the authors would like to emphasize again that in this paper, the main purpose of the SECM simulation was to study the influence of various geometrical parameters on the SECM resolution and finally to determine the highest possible resolution which can be obtained by the AFM-based SECM instrument. The simulation results showed that a micrometer resolution has been achieved, which is appreciated. The calibration sample did not give such a high-resolution distinction. The reason was that each gold band was a minimum 10 μm in width. Therefore, the simulation tools mostly have been employed for probe geometry design optimization. Unfortunately, a better calibration sample with less width down to 1–2 μm was not available. In our opinion, a normal AFM calibration sample with sharp edges like gold bands or grids is not an ideal sample for both AFM and SECM calibration. Therefore, the exact comparison between simulation and calibration sample results was not possible. It would be desirable to run the experiment with a better calibration sample. Therefore, the judgment was made from the highest possible SECM resolution based on the simulation results, estimated by the available calibration sample, and verified by the minimum distinguishable distances from actual measurement in real conditions (the AFM-SECM measurement has been employed for localized corrosion of aluminum alloys, but the results were not presented in this paper; they will be published later with more data achievement).

In summary, concurrent AFM and SECM images obtained on a gold band calibration sample verifies the high-resolution capability of the SECM of one or a few micrometers with optimized conditions.

Conclusions

An integrated AFM/SECM system has been developed for in situ studies of localized corrosion. A dual-mode probe acts as an AFM tip and SECM microelectrode simultaneously, to obtain concurrent topography and a current map of the very same surface area. Static and dynamic numerical simulations of the SECM part have been performed for two types of probes with different geometrical configurations.

By coupling Navier–Stokes momentum and mass balance equations, the influence of transient effects and of convective mass transport during the scanning were estimated. At normal scan rates (around 1 Hz), the results suggest that the Pt microelectrode collects a steady-state current, and the effect of convective transport of the mediator is negligible. The lateral resolution of the SECM measurement depends on electrochemical and geometrical parameters such as the Pt microelectrode size, sample–electrode distance, size of the active site, and the distance between two active sites. The simulations indicate that, under favorable conditions and probe geometry, two active sites 1 μm in size can be resolved in the SECM mapping if the distance between them is 3–4 μm or larger.

The paper also reports the experiments for characterization and calibration of the dual-mode probe with two probe geometries for verification of the performance and resolution of the AFM/SECM. Based on the results, it can be concluded that the instrument noise is less that 20 pA and the effective diameter of the Pt microelectrode is around 1–2 μm. Concurrent AFM topography and SECM electrochemical current images can be obtained on the same surface area. The SECM results are in good agreement with the numerical simulations, and the measurements on a calibration gold band surface verify micrometer lateral resolution under favorable conditions.

Acknowledgments

References

1. J. O. Park, C. H. Paik, Y. H. Huang, and R. C. Alkire, *J. Electrochem. Soc.*, **146**, 517 (1999).
2. A. Davoodi, J. Pan, C. Leygraf, and S. Norgren, *Appl. Surf. Sci.*, **252**, 5499 (2006).
3. M. Femenia, J. Pan, C. Leygraf, and P. Luukkonen, *Corros. Sci.*, **43**, 1939 (2001).
4. M. Femenia, J. Pan, and C. Leygraf, *J. Electrochem. Soc.*, **149**, B187 (2002).
5. P. P. Leblanc and G. S. Frankel, *J. Electrochem. Soc.*, **149**, B239 (2002).
6. D. O. Wipf, *Colloids Surf., A*, **93**, 251 (1994).
7. C. Gabrielli, S. Joiret, M. Keddam, H. Perrot, N. Portail, P. Rousseau, and V. Vivier, *Electrochim. Acta*, **52**, 7706 (2007).
8. C. H. Paik, H. S. White, and R. C. Alkire, *J. Electrochem. Soc.*, **147**, 4120 (2000).
9. M. Büchler, J. Kerimo, F. Guillaume, and W. H. Smyrl, *J. Electrochem. Soc.*, **147**, 3691 (2000).
10. J. C. Seegmiller and D. A. Buttry, *J. Electrochem. Soc.*, **150**, B413 (2003).
11. T. E. Lister and P. J. Pinhero, *Electrochem. Solid-State Lett.*, **5**, B33 (2002).
12. I. Serebrennikova and H. S. White, *Electrochem. Solid-State Lett.*, **4**, B4 (2001).
13. C. E. Gardner and J. V. Macpherson, *Anal. Chem.*, **74**, 576A (2002).
14. J. V. Macpherson, J. Z. Zhang, C. E. Gardner, and P. Unwin, *Anal. Sci.*, **17**, i333 (2001).
15. J. V. Macpherson and P. R. Unwin, *Anal. Chem.*, **72**, 276 (2000).
16. P. S. Dobson, J. M. R. Weaver, M. N. Holder, P. R. Unwin, and J. V. Macpherson, *Anal. Chem.*, **77**, 424 (2005).
17. J. V. Macpherson, C. E. Jones, A. L. Barker, and P. R. Unwin, *Anal. Chem.*, **74**, 1841 (2002).
18. J. V. Macpherson, J. Gueneau de Mussy, and J. Delplancke, *J. Electrochem. Soc.*, **149**, B306 (2002).
19. J. Gueneau de Mussy, J. V. Macpherson, and J. Delplancke, *Electrochim. Acta*, **48**, 1131 (2003).
20. C. Kranz, G. Friedbacher, B. Mizaikoff, A. Lugstein, J. Smoliner, and E. Bertagnolli, *Anal. Chem.*, **73**, 2491 (2001).
21. A. Lugstein, E. Bertagnolli, C. Kranz, and B. Mizaikoff, *Surf. Interface Anal.*, **33**, 146 (2002).
22. C. Kranz, A. Kueng, A. Lugstein, E. Bertagnolli, and B. Mizaikoff, *Ultramicroscopy*, **100**, 127 (2004).
23. M. R. Gullo, P. L. T. M. Frederix, T. Akiyama, A. Engel, N. F. deRooji, and U. Staufer, *Anal. Chem.*, **78**, 5436 (2006).
24. Y. Hirata, S. Yabuki, and F. Mizutani, *Bioelectrochemistry*, **63**, 217 (2004).
25. R. J. Fasching, Y. Tao, and F. B. Prinz, *Sens. Actuators B*, **108**, 964 (2005).
26. T. Nann and J. R. Heinze, *Electrochem. Commun.*, **1**, 289 (1999).
27. T. Nann and J. R. Heinze, *Electrochim. Acta*, **48**, 3975 (2003).
28. Q. Fulian, A. C. Fisher, and G. Denuault, *J. Phys. Chem. B*, **103**, 4387 (1999).
29. M. N. Holder, C. E. Gardner, J. V. Macpherson, and P. R. Unwin, *J. Electroanal. Chem.*, **585**, 8 (2005).
30. O. Sklyar and G. Wittstock, *J. Phys. Chem. B*, **106**, 7499 (2002).
31. O. Sklyar, J. Ufheil, J. Heinze, and G. Wittstock, *Electrochim. Acta*, **49**, 117 (2003).
32. O. Sklyar, A. Kueng, C. Kranz, B. Mizaikoff, A. Lugstein, E. B. G. Ertagnolli, and G. Wittstock, *Anal. Chem.*, **77**, 764 (2005).
33. O. Sklyar, M. Träuble, C. Zhao, and G. Wittstock, *J. Phys. Chem. B*, **110**, 15869 (2006).
34. P. A. Kottke and A. G. Federov, *J. Electroanal. Chem.*, **583**, 221 (2005).
35. A. Davoodi, J. Pan, C. Leygraf, and S. Norgren, *Electrochem. Solid-State Lett.*, **8**, B21 (2005).
36. A. Davoodi, J. Pan, C. Leygraf, and S. Norgren, *Electrochim. Acta*, **52**, 7697 (2007).
37. A. Davoodi, J. Pan, C. Leygraf, and S. Norgren, *J. Electrochem. Soc.*, **155**, C138 (2008).
38. A. Davoodi, J. Pan, C. Leygraf, and S. Norgren, *J. Electrochem. Soc.*, **155**, C211 (2008).
39. A. J. Bard, F. F. Fan, J. Kwak, and O. Lev, *Anal. Chem.*, **61**, 132 (1989).
40. A. J. Bard and M. V. Mirkin, *Scanning Electrochemical Microscopy*, 1st ed., Marcel Dekker, New York (2001).